ELSEVIER

Chemical Engineering Science 59 (2004) 3331–3343

Chemical Engineering Science

www.elsevier.com/locate/ces

Large-scale simulation of polymer electrolyte fuel cells by parallel computing

Hua Meng, Chao-Yang Wang*

Department of Mechanical and Nuclear Engineering, Electrochemical Engine Center (ECEC), The Pennsylvania State University, University Park, PA 16802, USA

Received 17 March 2003; received in revised form 8 January 2004; accepted 31 March 2004

Abstract

A three-dimensional, electrochemical–transport fully coupled numerical model of polymer electrolyte fuel cells (PEFC) is introduced. A complete set of conservation equations of mass, momentum, species, and charge are numerically solved with proper account of electrochemical kinetics and water management. Such a multi-physics model combined with the need for a large numerical mesh results in very intense computations that require parallel computing in order to reduce simulation time. In this study, we explore a massively parallel computational methodology for PEFC modeling, for the first time. The physical model is validated against experimental data under both fully and low-humidified feed conditions. Detailed results of hydrogen, oxygen, water, and current distributions in a PEFC of 5-channel serpentine flow-field are discussed. Under the fully humidified condition, current distribution is determined by the oxygen concentration distribution. Cell performance decreases in low-humidity inlet conditions, but good cell performance can still be achieved with proper water management. Under low-humidity conditions, current distribution is dominated by the water distribution at high cell voltages. When the cell voltage is low, the local current density initially increases along the flow path as the water concentration rises, but then starts to decrease due to oxygen consumption. Under both fully and low-humidified conditions, numerical results reveal that the ohmic losses due to proton transport in anode and cathode catalyst layers are comparable to that in the membrane, indicating that the catalyst layers cannot be neglected in PEFC modeling.

Keywords: Computational fuel cell dynamics (CFCD); Parallel computing; Water management; Polymer electrolyte fuel cell; Low humidity operation

1. Introduction

Polymer electrolyte fuel cells (PEFC) are considered as a promising alternative power source for transportation application because of their high efficiency, low emission, and low noise. In the past decade, significant improvements have been achieved in PEFC technology, including improved membrane-electrode assembly (MEA), and lowered platinum catalyst loading (Gottesfeld and Zawodzinski, 1997).

As in many engineering fields, numerical modeling and simulation becomes an important tool for enhancing physical understanding and optimizing designs of polymer electrolyte fuel cells. Many successful numerical models have been developed with increasingly less restrictive assumptions in the past decade. Early models (Bernardi and Verbrugge, 1991, 1992; Springer et al., 1991) were all based on the one-dimensional simplification. Modeling efforts were focused on electrochemical and transport phenomena in diffusion layers, catalyst layers, and membrane. Improvements were later made to consider gas concentration variations along the flow direction of gas channels. In these pseudo two-dimensional numerical models (Fuller and Newman, 1993; Nguyen and White, 1993; Yi and Nguyen, 1998), chemical species and local current density distributions along the channel direction were investigated, and water and thermal management were studied. Further developments in two-dimensional modeling of PEM fuel cells were in the direction of applying computational fluid dynamics (CFD) to establish complete flow fields in gas channels, diffusion and catalyst layers (Gurau et al., 1998; Um et al., 2000). Transport equations of chemical species were solved with source/sink terms arising from electrochemical kinetics.

* Corresponding author. Tel.: +1-814-863-4762; fax: +1-814-863-4848.
E-mail address: cxw31@psu.edu (C.-Y. Wang).

0009-2509/$ - see front matter © 2004 Elsevier Ltd. All rights reserved.
doi:10.1016/j.ces.2004.03.039

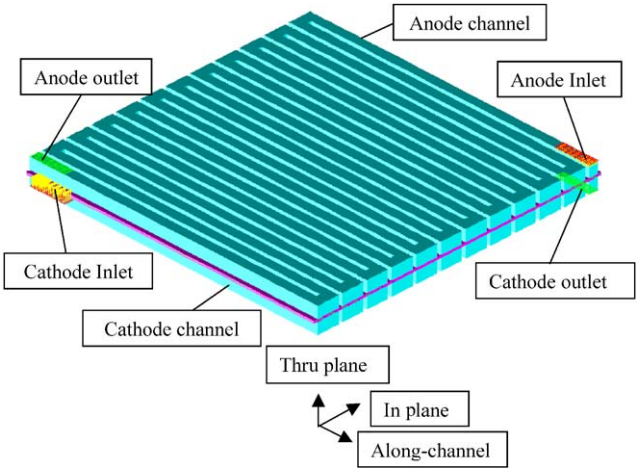

Fig. 1. Large-scale polymer electrolyte fuel cell.

An additional charge conservation equation was solved to predict the electrolyte phase potential distribution inside the MEA. Dependences of the membrane water diffusivity and proton conductivity on water content were treated using the empirical correlations of Springer et al. (1991). Good agreement was reached between numerical and experimental results. Research efforts have recently been made towards modeling PEFCs in three dimensions (Dutta et al., 2000, 2001; Um and Wang, 2000; Zhou and Liu, 2001). In these numerical models, conservation equations of mass, momentum, and species were solved in gas channels and diffusion layers, while electrochemical kinetics was taken into account by source/sink terms in species and charge equations. Local current distribution and flow field characteristics were investigated. In the models of Dutta et al. (2000, 2001), the membrane electrode assembly (MEA) was not included in the computational domain, but rather simplified as an interface without thickness. As such, water transport and ohmic potential drop across MEA were treated using simplified linear relationships as in the early work of Nguyen and White (1993). Since the electrochemical and transport phenomena inside MEA are critically important for physical understanding and engineering design of high-performance high-reliability fuel cells, a three-dimensional numerical model, capable of revealing details of water and electrolyte potential distributions inside MEA as well as ohmic losses of proton transport across catalyst layers, is necessary.

Despite these recent advances in PEFC modeling, physical and computational challenges still lie ahead. One computational challenge is the need for a large numerical mesh in order to simulate industrial-scale fuel cells. Past simulations were all restricted to cells with either small size or few features. To fully appreciate the large mesh needed for fuel cell modeling, consider a typical geometry of a large-scale PEFC, displayed in Fig. 1, where the anode flow-field (on the top) and cathode flow-field (on the bottom) sandwich a MEA with two gas diffusion layers (GDL). Lets define the through-plane direction to be perpendicular to the MEA, the along-channel direction to be of main gas flow, and the in-plane direction to be across channels through the land area. Suppose that 6–8 grid-points are needed to sufficiently resolve each of the five distinctive regions of MEA and two GDLs, and 10 grid-points needed in each of the two gas channels, the minimum number of grid-points in the through-plane dimension is thus between 50 and 60. In the along-channel direction, 100 grid-points are typically required since fuel cell channels are long and exhibit a large aspect ratio (>100). In the in-plane direction, ten nodal points are needed for a channel and a land, respectively, thus giving rise to 20 grid-points per channel within a flow-field. For large-scale fuel cells featuring twenty- to sixty-channel flow-field, a mesh consisting of two to six million grid-points is needed. All numerical work published to date have used no more than a few hundreds of thousands computational cells; that is, there is still one order of magnitude gap existing between the current computational capability and what is needed for high-fidelity PEFC simulation. The present study aims to bridge this gap by developing a massively parallel computational methodology based on the efficient domain decomposition method.

In this paper, a three-dimensional electrochemical–transport fully coupled numerical model for PEFC is presented. Conservation equations of mass, momentum, and species in gas channels, diffusion and catalyst layers, and a charge conservation equation inside MEA (including catalyst layers and membrane) are solved numerically. Water uptake and diffusion in MEA are properly accounted, as well as electro-osmosis. Electrochemical reactions, including hydrogen oxidation reaction (HOR) in the anode catalyst layer and oxygen reduction reaction (ORR) in the cathode catalyst layer, are taken into account by adding proper source/sink terms in species and charge conservation equations. The transfer current densities are calculated using the Butler–Volmer equation. This PEFC model is then implemented into a commercial CFD package, Star-CD, using its user-coding capability (Star-CD, 2001). The user code is fully parallelized using the efficient domain decomposition method for large-scale PEFC simulations, and the computational speed-up using parallel computing is quantified. For the first time, large-scale computations with numerical mesh of the order of 10^6 gridpoints have been carried out.

The parallelized fuel cell model was used to investigate the performances of a PEFC with five-channel serpentine flow-field at both fully humidified gas feed and low humidity operations. In transportation applications, it is not practical to carry a large on-board humidifier to fulfill full humidification of both anode and cathode gas feed. Since the PEFC performance strongly depends on MEA hydration, recent research efforts are therefore directed towards improving PEFC performance under low-humidity operation, especially on the cathode side where a large amount of water will be produced through the electrochemical reaction

Table 1
Conservation equations

	Conservation equations	Source terms
Mass	$\nabla \cdot (\rho \vec{u}) = 0$ (1)	
Momentum	$\frac{1}{\varepsilon^2}\nabla \cdot (\rho \vec{u}\vec{u}) = -\nabla p + \nabla \cdot \tau + S_u$ (2)	In diffusion and catalyst layers: $S_u = -\frac{\mu}{K}\vec{u}$
Species concentration	$\nabla \cdot (\vec{u}c_i) = \nabla \cdot (D_i^{\text{eff}} \nabla c_i) + S_i$ (3)	In catalyst layers: $S_i = -\frac{s_i j}{nF}$ for hydrogen and oxygen; $S_i = -\nabla \cdot \left(\frac{n_d}{F} i_e\right) - \frac{s_i j}{nF}$ for water in MEA
Charge	$\nabla \cdot (\kappa^{\text{eff}} \nabla \phi_e) + S_\phi = 0$ (4)	In catalyst layers: $S_\phi = j$

Electrochemical reactions:

$\sum_i s_i M_i = ne^-$ where $M_i \equiv$ chemical formula of species; $s_i \equiv$ stoichiometry coefficient; $n \equiv$ number of electrons transferred

Hydrogen oxidation reaction in anode side : $H_2 - 2H^+ = 2e^-$ (5)

Oxygen reduction reaction in cathode side : $2H_2O - O_2 - 4H^+ = 4e^-$ (6)

and transported via electro-osmotic drag. Furthermore, low humidity of the cathode inlet could also lessen the possible cathode flooding problem.

This paper is arranged as follows: the 3-D numerical model is introduced in Section 2, along with detailed physicochemical and transport parameters; numerical results for a PEFC with 5-channel serpentine flow-field are discussed in Section 3, including numerical validation against experimental data; and major findings are summarized in Section 4.

2. Numerical model

In this section, a three-dimensional single-phase isothermal model of PEFC is presented, which is capable of investigating electrochemical and transport phenomena in all seven regions of a PEFC, namely gas channels, diffusion and catalyst layers in both anode and cathode sides, and membrane, as shown in Fig. 2. Conservation equations of mass, momentum, chemical species, and charge, as presented in Table 1, are numerically solved, with proper account of electrochemical kinetics. Superficial velocities are used in the momentum equations in order to automatically ensure mass flux continuity at the interface between the porous GDL and non-porous gas channel.

The mass and momentum equations are numerically solved to obtain the flow field. The source terms in the momentum equations are added based on the Darcy's law, representing an extra drag force proportional to fluid viscosity and velocity, and inversely proportional to the permeability of a porous medium. This treatment will lead to the exact

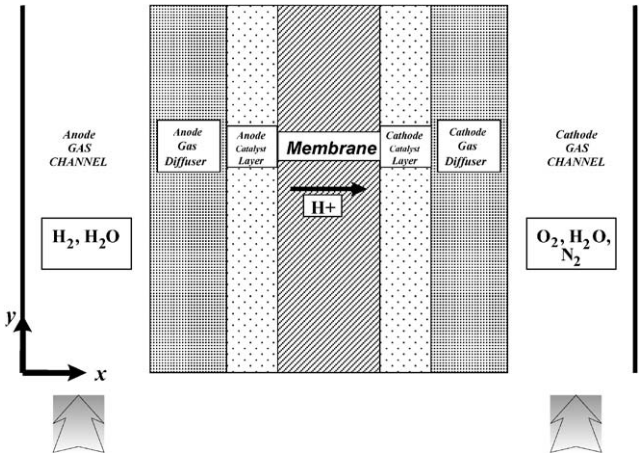

Fig. 2. Model schematic of a polymer electrolyte fuel cell.

Darcy's equation as the velocity in porous media becomes extremely small, rendering negligible inertial and viscous terms in the momentum equations. The species concentration equations are solved to obtain hydrogen, oxygen, and water distributions, in which the source terms are implemented based on electrochemical kinetics. An additional charge conservation equation is solved to take into account of proton transport inside MEA.

The single phase assumption for water transport in this model implies that water can exist in super-saturation in the gas phase or if condensed, liquid water exists as finely dispersed droplets as in a mist flow and produces negligible effects on the gas phase transport. That is, the water

activity calculated based on water partial pressure is allowed to be greater than unity (Springer et al., 1991). As shown later in this paper, effect of water over-saturation on water uptake and back-diffusion in MEA is properly accounted through Springer's empirical correlations. Phase change and cathode flooding, however, cannot be addressed by such a single-phase model and requires a two-phase formulation where liquid water transport and hydrophobicity effects in gas diffusion layers are fully accounted for (Wang, et al., 2001; Wang, 2003).

Electrochemical reactions in a PEFC, including the hydrogen oxidation reaction (HOR) and oxygen reduction reaction (ORR), are accounted for using proper source/sink terms in the species and charge concentration equations. The transfer current densities in these equations are expressed by the modified Butler–Volmer equation in the anode and cathode, respectively, as

$$\textit{Anode}: \quad j = a j_{0,a}^{\text{ref}} \left(\frac{c_{\text{H}_2}}{c_{\text{H}_2,\text{ref}}} \right)^{1/2} \left(\frac{\alpha_a + \alpha_c}{RT} \cdot F \cdot \eta \right), \tag{7}$$

$$\textit{Cathode}: \quad j = -a j_{0,c}^{\text{ref}} \left(\frac{c_{\text{O}_2}}{c_{\text{O}_2,\text{ref}}} \right) \exp\left(-\frac{\alpha_c}{RT} \cdot F \cdot \eta \right), \tag{8}$$

where all the parameters are presented in Table 4. On the anode side, the Butler–Volmer equation is linearized based on the fact of facile HOR kinetics or small overpotential. The overpotentials are defined as

$$\textit{Anode side}: \quad \eta = -\phi_e \tag{9}$$

$$\textit{Cathode side}: \quad \eta = V_{\text{cell}} - \phi_e - U_{\text{oc}} \tag{10}$$

where V_{cell} represents the operation cell voltage, and U_{oc} is the open-circuit potential defined as (Berger, 1968)

$$U_{\text{oc}} = 1.23 - 0.9\times10^{-3}(T - 298) + \frac{RT}{2F}(\ln p_{\text{H}_2} + \frac{1}{2}\ln p_{\text{O}_2}) \tag{11}$$

The ohmic loss due to electron transport in catalyst and gas diffusion layers has been neglected in deriving the two overpotential equations, Eqs. (9) and (10). Details about the electrolyte phase potential, ϕ_e, determined by solving a charge conservation equation, Eq. (4) in Table 1, are discussed later in this section.

In the water transport equation, the second source term is added in the cathode catalyst layer based on water generation from ORR reaction. Water transport caused by electro-osmotic drag is treated as an additional source/sink term in the entire MEA region, presented as the first source term in Eq. (3) of Table 1. Here n_d stands for the electro-osmotic drag coefficient (Springer et al., 1991), i.e.

$$n_d = \frac{2.5\lambda}{22} \tag{12}$$

The water concentration in the membrane is defined as

$$c_w^m = \frac{\rho_{\text{dry}}\lambda}{\text{EW}} \tag{13}$$

where ρ_{dry} and EW represent the dry membrane density and its equivalent molecular weight, respectively.

Membrane water content, defined as water molecules per sulfonic-acid group (SO_3^-), is determined by the water activity at the interface of membrane and gas phases in thermodynamic equilibrium. Water activity in the gas phase is calculated by

$$a = \frac{C_w RT}{p^{\text{sat}}} \tag{14}$$

where the saturation pressure of water was fitted to tabular data using the following expression (Springer et al., 1991):

$$\begin{aligned} \log_{10} p^{\text{sat}} = {} & -2.1794 + 0.02953(T - 273.15) \\ & -9.1837\times10^{-5}(T - 273.15)^2 \\ & +1.4454\times10^{-7}(T - 273.15)^3 \end{aligned} \tag{15}$$

An empirical formulation (Springer et al., 1991), correlating membrane water content with water activity, is employed in this model, in which the existence of liquid water is considered using a linear relationship above water activity of unity.

$$\lambda = \begin{cases} 0.043 + 17.18a - 39.85a^2 + 36.0a^3 & 0 < a \leqslant 1, \\ 14 + 1.4(a - 1) & 1 < a \leqslant 3. \end{cases} \tag{16}$$

Membrane water diffusivity is calculated using the following relationship of Motupally et al. (2000):

$$D_w^m = \begin{cases} 3.1\times10^{-7}\lambda(\text{e}^{0.28\lambda} - 1)\text{e}^{[-2346/T]} & 0 < \lambda \leqslant 3, \\ 4.17\times10^{-8}\lambda(1 + 161\text{e}^{-\lambda})\text{e}^{[-2346/T]} & \text{otherwise}. \end{cases} \tag{17}$$

A charge conservation equation, Eq. (4) in Table 1, is solved to describe proton transport inside MEA. The dependence of proton conductivity on water content is calculated using the following empirical expression of Springer et al. (1991):

$$\kappa = (0.5139\lambda - 0.326)\exp\left[1268\left(\frac{1}{303} - \frac{1}{T}\right)\right]. \tag{18}$$

The effective mass diffusivity and proton conductivity in porous media are treated using the Bruggeman relation

$$D_i^{\text{eff}} = D_i \varepsilon^{1.5}, \quad \kappa^{\text{eff}} = \kappa\varepsilon^{1.5}. \tag{19}$$

Local current density on the membrane is calculated by

$$I = -\kappa^{\text{eff}} \nabla\phi. \tag{20}$$

Table 2
Physicochemical properties and relations

Description	Expression	Unit
Transfer current density	$j = aj_{0,a}^{\text{ref}} \left(\frac{c_{\text{H}_2}}{c_{\text{H}_2,\text{ref}}}\right)^{1/2} \left(\frac{\alpha_a + \alpha_c}{RT} \cdot F \cdot \eta\right)$ in anode (7)	A/m^3
	$j = -aj_{0,c}^{\text{ref}} \left(\frac{c_{\text{O}_2}}{c_{\text{O}_2,\text{ref}}}\right) \exp\left(-\frac{\alpha_c}{RT} \cdot F \cdot \eta\right)$ in cathode side (8)	
Over potential	$\eta = -\phi_e$ in anode side (9)	V
	$\eta = V_{\text{cell}} - \phi_e - U_{\text{oc}}$ in cathode side (10)	
Open-circuit potential	$U_{\text{oc}} = 1.23 - 0.9 \times 10^{-3}(T - 298) + \frac{RT}{2F}\left(\ln p_{\text{H}_2} + \frac{1}{2}\ln p_{\text{O}_2}\right)$ (11)	V
Electro-osmotic drag coefficient	$n_d = \frac{2.5\lambda}{22}$ (12)	
Water concentration in membrane	$c_w^m = \frac{\rho_{\text{dry}}\lambda}{\text{EW}}$ (13)	mol/m^3
Water activity	$a = \frac{C_w RT}{p^{\text{sat}}}$ (14)	
Water saturation pressure	$\log_{10} p^{\text{sat}} = -2.1794 + 0.02953(T - 273.15) - 9.1837 \times 10^{-5}(T - 273.15)^2 + 1.4454 \times 10^{-7}(T - 273.15)^3$ (15)	atm
Water content	$\lambda = \begin{cases} 0.043 + 17.18a - 39.85a^2 + 36.0a^3 & 0 < a \leqslant 1 \\ 14 + 1.4(a-1) & 1 < a \leqslant 3 \end{cases}$ (16)	
Membrane water diffusivity	$D_w^m = \begin{cases} 3.1 \times 10^{-7}\lambda(\text{e}^{0.28\lambda} - 1)\text{e}^{[-2346/T]} & 0 < \lambda \leqslant 3 \\ 4.17 \times 10^{-8}\lambda(1 + 161\text{e}^{-\lambda})\text{e}^{[-2346/T]} & \text{otherwise} \end{cases}$ (17)	m^2/s
Proton conductivity	$\kappa = (0.5139\lambda - 0.326)\exp\left[1268\left(\frac{1}{303} - \frac{1}{T}\right)\right]$ (18)	S/m
Effective diffusivity/conductivity	$D_i^{\text{eff}} = D_i\varepsilon^{1.5}, \quad \sigma^{\text{eff}} = \sigma\varepsilon^{1.5}$ (19)	m^2/s

The average current density over the membrane area is given by

$$I_{\text{avg}} = \frac{1}{A}\int_A I \, \text{d}A, \tag{21}$$

where I is the local current density on the membrane and A is the membrane area.

The conservation equations and their supplemental relationships are summarized in Tables 1 and 2, respectively. This PEFC numerical model is implemented into a commercial computational fluid dynamics (CFD) package, Star-CD, basing on its user-coding capability (Star-CD, 2001). The user code is run in parallel using the domain decomposition method and message passing interface (MPI) and is made computationally efficient.

3. Results and discussion

The numerical model is first validated against experimental data from Toyota Motor Corp. (2002) at both full- and low-humidity conditions. Fig. 3 presents the polarization curves from the computational results against the experimental data. Excellent agreement is reached for both cases.

In this study, the parallel computational model is applied to investigate the performance of a PEFC with 5-channel serpentine flow-field. The key geometric parameters are presented in Table 3. A total of one million computational cells are required for numerical calculations, based on grid-independence study. All numerical calculations are carried out in an in-house Linux PC cluster comprising of 50 processors of 1.4 GHz AMD Athelon Thunderbird CPU and 512 MB DDR SDRAM. A local 100 Mbps switched Ethernet network is used for message communication. Fig. 4 presents the computational performance of the PC cluster, demonstrating more than 7× speed-up by 10 CPUs running the massively parallelized PEFC model. Roughly 300 iterations are needed for a typical case run, requiring about 1.5 h of computational time using 10 CPUs. This clearly demonstrates the effectiveness of parallel computing in reducing actual computing time for these intensive simulations.

To explore PEFC characteristics under low-humidity operation, four simulation cases are designed, as shown in Table 5. Case 1 represents the PEFC operated at the fully

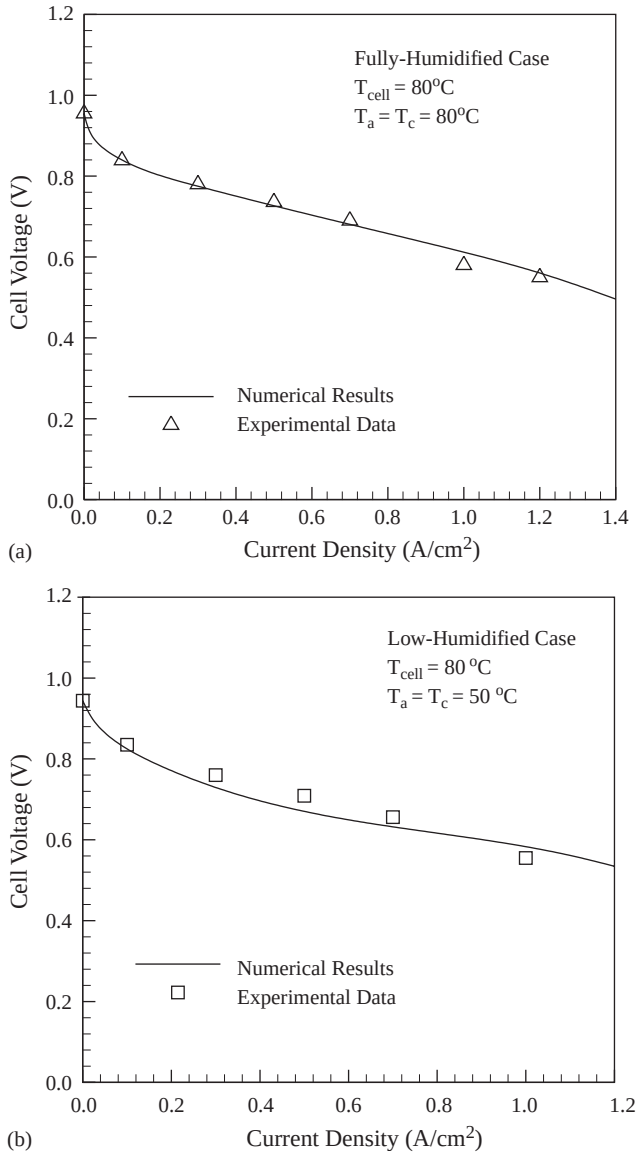

Fig. 3. Model validation: (a) under fully humidified inlet conditions, and (b) under low-humidified inlet conditions.

humidified inlet conditions in both anode and cathode inlets (i.e. a baseline case), case 2 with fully humidified anode inlet but dry cathode inlet (relative humidity of 5%), case 3 with the relative humidity of 26% in both anode and cathode sides, case 4 at anode relative humidity of 26% but dry cathode inlet. In all cases, the fuel cell operates at 80°C and 2 atm. The mixture of hydrogen and water flows into the anode inlet, while air and water through the cathode inlet. A stoichiometry of 2 at a reference current density of 1 A/cm^2 is defined in both anode and cathode inlets; that is, these are constant flow rates equivalent to 2 A/cm^2. A total contact resistance of 40 mΩ cm^2 is included in the present numerical calculations. The electrochemical and transport parameters used in the present numerical investigation are summarized in Table 4.

Table 3
Cell geometry

Fuel cell geometry (mm)	
Cell length	70.00
Gas channel	
Depth	2.500
Width	1.500
Layer thickness	
Diffusion	0.300
Catalyst	0.010
Membrane	0.025
Land width	0.750
Computational cell numbers for 5-channel cell	$\sim$ 1 million

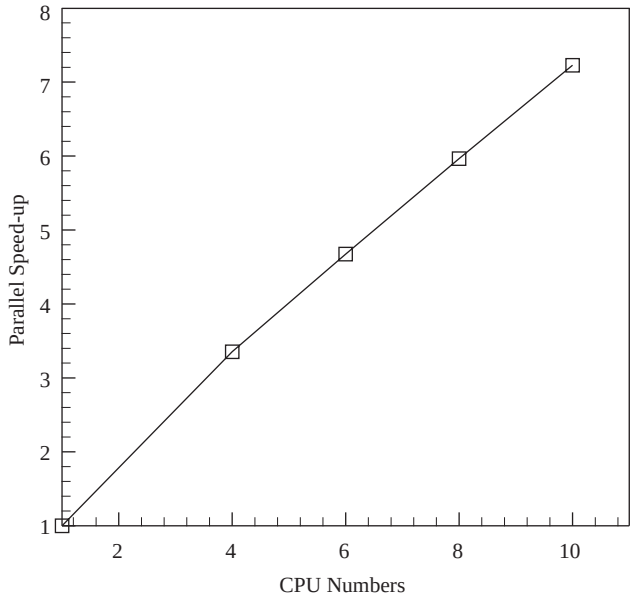

Fig. 4. Computational speed-up by parallel computing using a Linux PC cluster.

Table 4
Electrochemical and transport parameters

Anode total exchange current density, aj_0 (A/m^3)	1.0E+9
Cathode total exchange current density, aj_0 (A/m^3)	1.0E+4
Reference hydrogen concentration, C_{H_2} (mol/m^3)	40
Reference oxygen concentration, C_{O_2} (mol/m^3)	40
Anode transfer coefficient	$\alpha_a = \alpha_c = 1$
Cathode transfer coefficient	$\alpha_c = 1$
Faraday constant, F	96487
Porosity of diffusion layer	0.6
Porosity of catalyst layer	0.112
Volume fraction of ionomer in catalyst layer	0.4
Permeability of the diffusion layer (m^2)	1.0E−15
Equivalent weight of ionomer (kg/mol)	1.1
Dry membrane density (kg/m^3)	1980
Universal gas constant (J/mol K)	8.314

Fig. 5 presents the polarization and power density curves from the four cases. Results indicate that cell performance decreases under low-humidity inlet conditions. In order to

achieve a power density of 0.5 W/cm^2, the fuel cell can operate at a cell voltage of 0.7 V in the fully humidified inlet conditions (case 1 in Table 5). The operational cell voltage will have to decrease to about 0.66 V when the relative humidity in the cathode inlet decreases to 5% (case 2 in Table 5). It will further decrease to 0.62 and 0.56 V in Cases 3 and 4 at even lower humidified inlet conditions. Since cell energy efficiency decreases with the decrease of cell voltage, it is better to maintain the cell voltage of a PEM fuel cell above 0.6 V during normal operation, corresponding to the overall cell efficiency above 40%. A PEM fuel cell operating with inlet conditions in Cases 2 and 3 is therefore preferred. In order to further improve cell performance in low-humidity operation, special design techniques have to be adopted, such as using stoichometry- controlled flow rates to avoid membrane dryout at low current densities or a counter-flow configuration between the anode and cathode, etc.

In Fig. 5, the increase of the mass-transfer-limited current densities under low-humidity conditions results from the high oxygen molar concentrations at the cathode inlet. At the same operation temperature and pressure, the total molar concentration in the cathode inlet stream remains the same for all the four cases. While the water concentration decreases in low-humidity gas feed, the oxygen molar concentration will increase. Furthermore, at low cell voltage and high current density, water production on the cathode side is sufficient to maintain good proton conductivity for all the simulated cases.

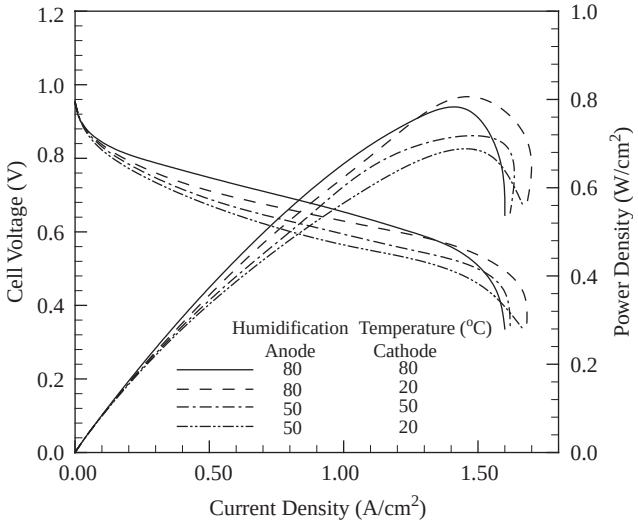

Fig. 5. Polarization and power density curves in four different humidification conditions.

Fig. 6a depicts the variation of the average oxygen molar concentration in the cathode catalyst layer under each gas channel at the fully humidified gas feed (case 1). There is a significant increase of oxygen concentrations in the U-turn regions caused by flow recirculation and reactant well-mixing. The effect is stronger on the cathode side because of the much larger gas velocity (about 4–5 times larger). Current density variation averaged under each gas channel is presented in Fig. 6b. The higher current density in each U-turn region is consistent with the higher oxygen concentration. Since the increase of hydrogen concentration under each U-turn region is not as significant as the oxygen concentration, the higher current density under each U-turn region demonstrates the dominant effect of the oxygen concentration on chemical kinetics, and thus cell performance at fully humidified conditions.

Fig. 7 presents the distributions of oxygen molar concentration in cathode catalyst layers under each gas channel in Cases 2 and 3, respectively. Cell voltages in both cases are at 0.67 V. Oxygen concentrations decrease from channel 1 to channel 5 in both cases, except in the U-turn regions, where the sharp increase of oxygen concentration results from flow field recirculation and reactant well-mixing, the same phenomenon shown in Fig. 6a.

Fig. 8 presents water distributions in the anode catalyst layer under gas channels in Cases 2 and 3 at a cell voltage of 0.67 V. In Case 2, Fig. 8a shows that water activity under the first gas channel decreases significantly. This is caused by two reasons: water loss from the anode to cathode by electro-osmotic drag and water diffusion also from the anode to cathode. Since the cathode side is relatively dry in this part of the cell, water forward-diffusion prevails. From channel 2 on, water activity begin to increase on the anode side, indicating that water back-diffusion from the cathode to anode becomes dominating with more water produced from the oxygen reduction reaction (ORR) in the cathode catalyst layer. In

Table 5
Inlet humidification temperatures and relative humidity at cell temperature of 80°C

Case number	Anode		Cathode	
	Humidification temperature (°C)	Relative humidity (%)	Humidification temperature (°C)	Relative humidity (%)
1	80	100	80	100
2	80	100	20	5
3	50	26	50	26
4	50	26	20	5

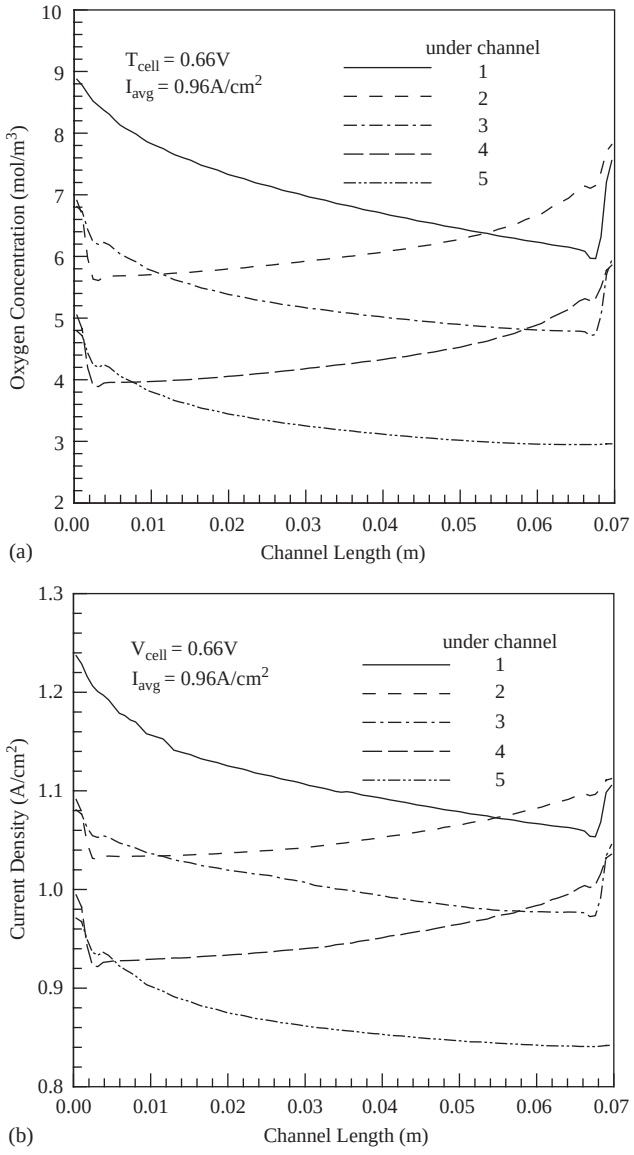

Fig. 6. (a) Variations of average oxygen molar concentration in cathode catalyst layer under gas channel, (b) Variations of the average current density under gas channels ($V_{cell} = 0.66$ V, $I_{avg} = 0.96$ A/cm^2).

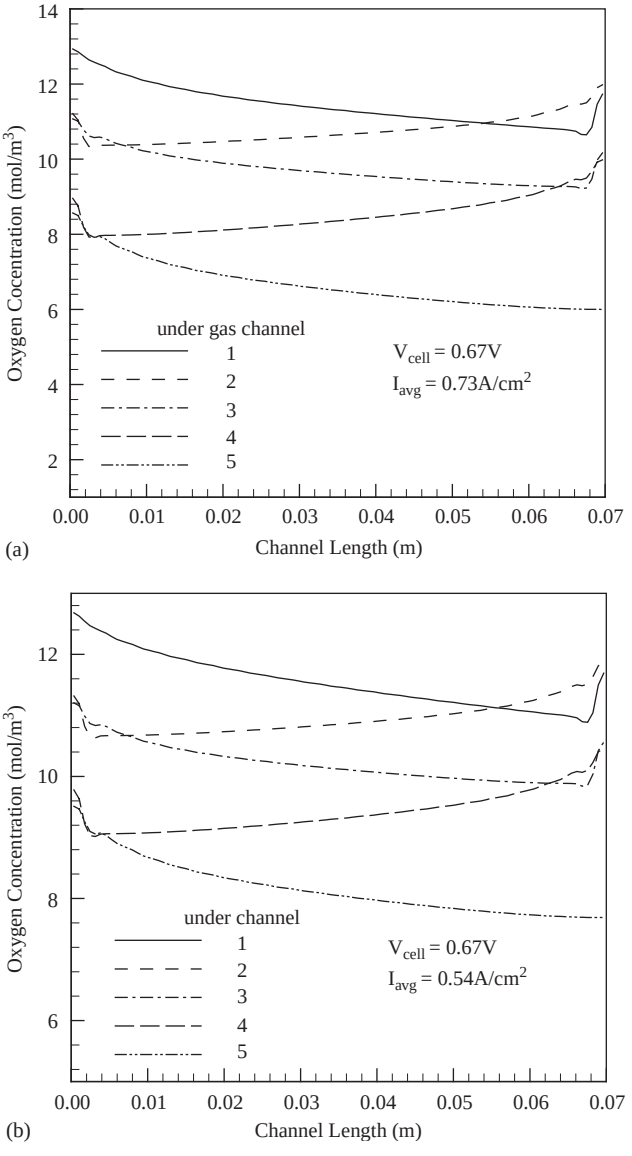

Fig. 7. Oxygen concentration profiles in the cathode catalyst layer under five gas channels: (a) in case 2, and (b) in case 3.

Case 3, Fig. 8b shows that the water concentration always increase, a phenomenon dominated by water back-diffusion. In this case, the amount of water transferred from the anode to cathode side by electro-osmotic drag is smaller because the relatively drier inlet condition results in lower current density under the first gas channel, compared with Case 2. Furthermore, since the water concentrations in both anode and cathode inlets are the same, water production on the cathode side easily results in water back-diffusion.

Water activities in the anode catalyst layer under the fifth gas channel at different operation cell voltages in Cases 2 and 3 are presented in Fig. 9. Results indicate that, at the anode outlet, water concentration increases at low cell voltage and high current density, demonstrating the strong effect of water back-diffusion from the cathode to anode side. In both cases, results show that no liquid exists in the anode side.

Fig. 10 shows water distributions in cathode catalyst layers under gas channels in Case 2. Water concentrations increase from channel 1 to 5, due to water production in oxygen reduction reaction (ORR) in the cathode catalyst layer. The sharp decreases of water concentration in U-turn regions are related to flow recirculation and water well-mixing in the gas channel. As shown in Fig. 10, at a cell voltage of 0.67 V, water activity is below unity, indicating no liquid water exists in the cathode. The same results are discovered in Cases 3 and 4.

Current density distributions in the middle of the membrane under gas channels are presented in Fig. 11. In Case 2, because of the fully humidified anode inlet and thereafter

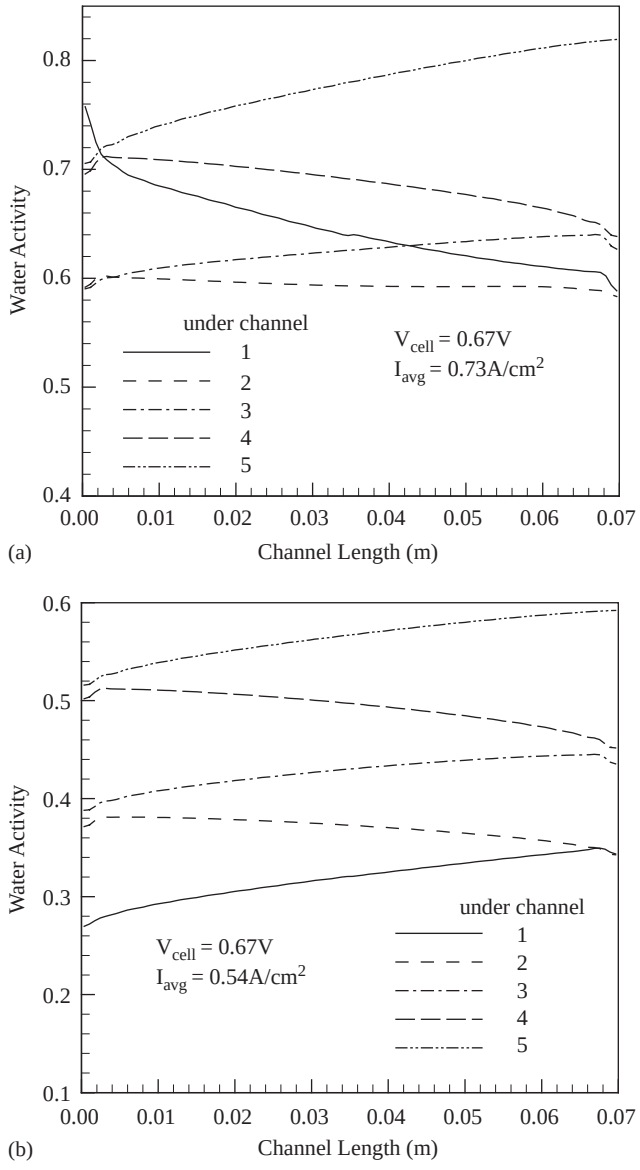

Fig. 8. Water activity profiles in the anode catalyst layer under five gas channels: (a) in case 2, and (b) in case 3.

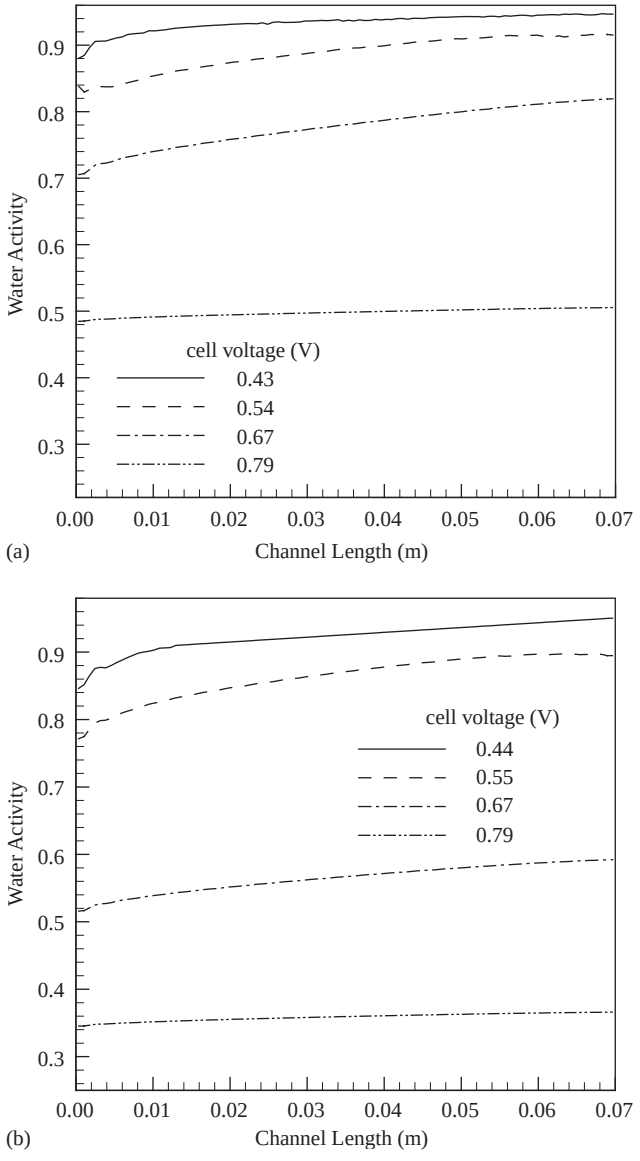

Fig. 9. Water activity profiles in the anode catalyst layer under the fifth gas channel at four different cell voltages: (a) in case 2, and (b) in case 3.

water redistribution from the anode to cathode side by electro-osmotic drag, Fig. 11a shows the current density near the cell inlet is high. The high current density under the first and second gas channels is sustained with only slight decrease due mainly to high oxygen concentration. From the third gas channel on, current density increases significantly because of a large amount of water produced on the cathode side and, in the mean time, diffusing into the anode side. The current distribution in this case is controlled by the membrane resistance instead of oxygen concentration. The same trend of current density increase also appears in Case 3, as shown in Fig. 11b, where current density increases from the first gas channel on. The dominant effect of water distribution on the current distribution in low-humidity operation in Cases 2 and 3 is different from that under full humidification. In the fully humidified inlet condition, current density decreases from the first gas channel on, showing the dominant effect of oxygen depletion on current density, Fig. 6b. Contour plots of current density distributions in Cases 2 and 3 are displayed in Fig. 12.

Fig. 13 presents current density distributions in the middle of the membrane under gas channels at a cell voltage of 0.55 V in case 3. From the first to the third gas channel, current density increases due to the dominant effect of water production and redistribution. However, from the fourth channel on, current density starts to decrease although there is more water in this part of the cell. Water distribution on the cathode side is presented in Fig. 14. The decrease of current density at low cell voltage is caused by the decrease of oxygen concentration. Because the current density under the first

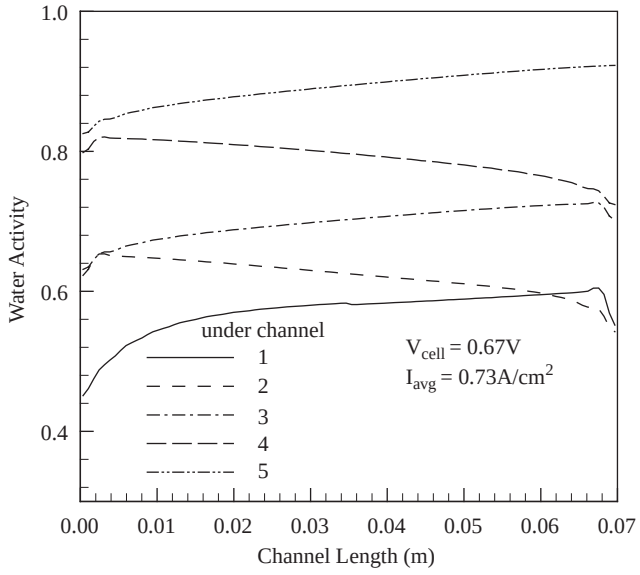

Fig. 10. Water activity profiles in the cathode catalyst layer under five gas channels in case 2.

three channels maintains high values, a large amount of oxygen is consumed in this part of the cell. The oxygen concentration in the last two channels becomes insufficient to sustain the high level of current density. Further decreasing the cell voltage, the current density starts to decrease at an even earlier stage. The same phenomena are observed in other cases of low-humidity gas feed (Cases 2 and 4 in Table 5). Fig. 14 shows that water activity toward the cathode outlet is above unity, possibly forming liquid water. However, the water activity in this case is much lower than that at the fully humidified gas feed, indicating that cathode flooding can indeed be lessened under low-humidity operation.

Fig. 15 presents electrolyte phase potential distributions across MEA under the middle of three gas channels in Case 3. The overpotentials at the anode side are very small because of the fast electrochemical kinetics of the anode reaction. From the first to the fifth gas channel, the overpotential in anode side decreases with the decrease of hydrogen concentration, demonstrating hydrogen dilution effect. As shown in Fig. 15, the gradient of phase potential decreases from the first to the fifth gas channel, although the current density increases in that direction. It is verified that, in this case, current density increase is indeed results from the increase of membrane water content and consequently, the increase of the proton conductivity. Furthermore, results in Fig. 15 reveal that the ohmic losses of proton transport in anode and cathode catalyst layers are comparable to that in the membrane under low-humidity operation, indicating that the catalyst layers cannot be neglected in numerical modeling of polymer electrolyte fuel cells. The same conclusion was also reached for a PEFC operated with fully humidified gas feed.

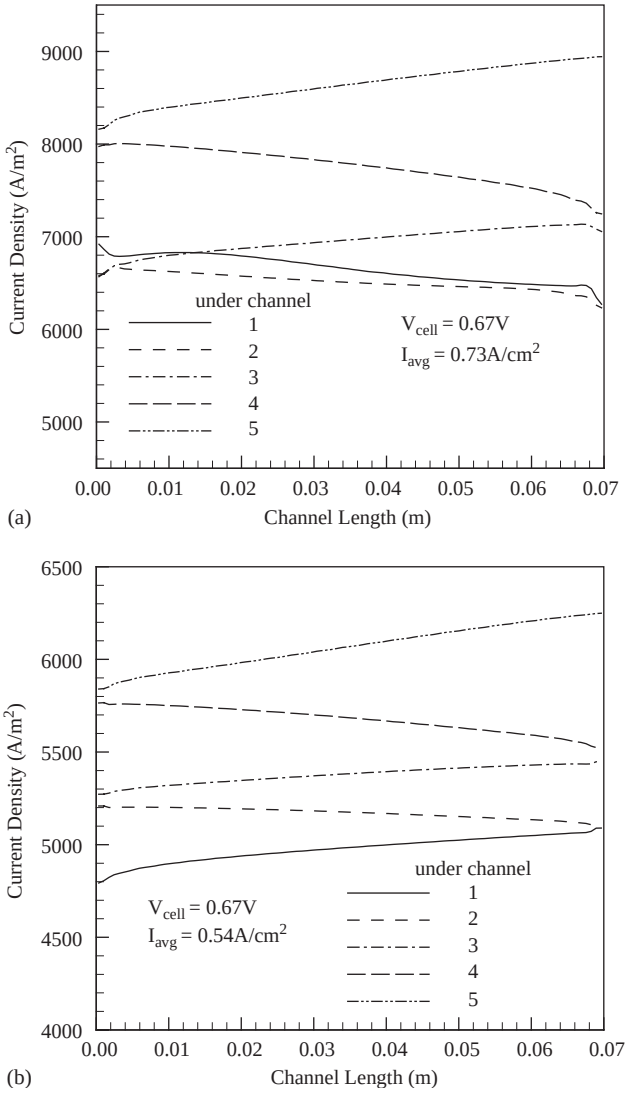

Fig. 11. Current density distribution in the middle of membrane under five gas channels: (a) in case 2, and (b) in case 3.

4. Conclusions

A three-dimensional, single-phase, electrochemical–transport fully coupled numerical model of polymer electrolyte fuel cells (PEFC) is introduced, which is capable of investigating electrochemical and transport phenomena in all seven regions of a PEM fuel cell, including anode gas channel, anode diffusion layer, anode catalyst layer, membrane, cathode catalyst layer, cathode diffusion layer, and cathode gas channel. A complete set of conservation equations of mass, momentum, species, and charge is numerically solved, with proper account of electrochemical kinetics and water management, including electro-osmosis, water back-diffusion across the membrane, and water production due to ORR in the cathode catalyst layer. The present PEFC model is built into a commercial computational fluid dynamic (CFD) package, Star-CD, through

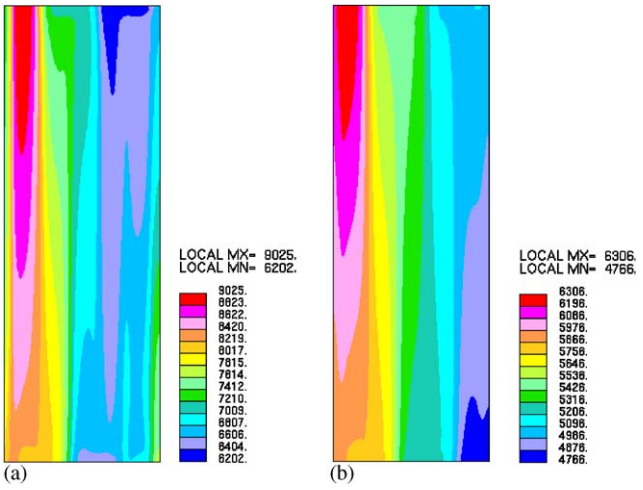

Fig. 12. Contour plot of current density (A/m^2) distribution in the middle of membrane: (a) in case 2, and (b) in case 3.

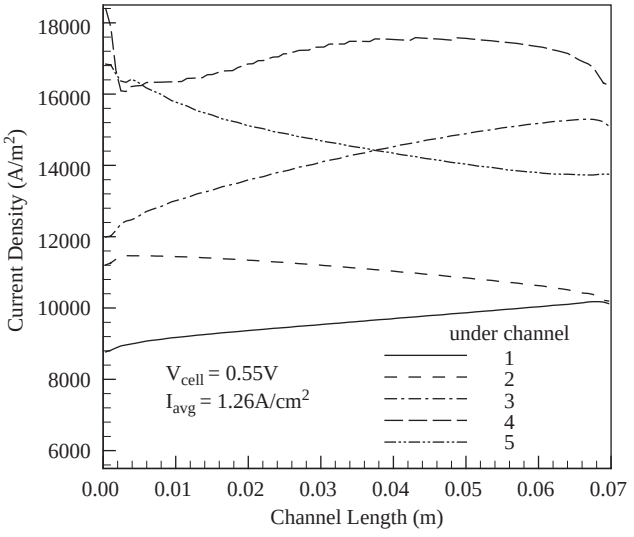

Fig. 13. Current density distributions in the middle of membrane under five gas channels at a cell voltage of 0.55 V in case 3.

its user-coding capability. The user code is fully parallel compatible and computationally efficient.

Numerical results are validated against experimental data under both full- and low-humidity conditions, demonstrating numerical accuracy of the present PEFC model. Numerical calculations are carried out in an in-house Linux PC cluster. The computational performance of the PEM fuel cell model on the PC cluster is quantified, demonstrating more than 7× speed-up using 10 CPUs. Roughly 300 iterations are needed for a typical case-run, requiring 1.5 hours of computational time for one million computational cells using 10 CPUs.

A PEFC of 5-channel serpentine flow-field operating at both fully humidified gas feed and low humidity conditions is numerically investigated. Detailed results of hydrogen, oxygen, water, and current distributions are discussed. Current distribution is determined by oxygen concentration on the cathode side at the fully humidified gas feed. Cell performance decreases under low-humidity operation, but good cell performance can still be achieved with properly designed low relative humidity range, including the fully humidified anode inlet but dry cathode inlet, and both low-humidified anode and cathode inlets at a relative humidity of 26 percent. In both cases, a polymer electrolyte fuel cell can operate at cell voltages above 0.6 V while maintaining the power density above 0.5 W/cm^2. Furthermore, numerical results show that cathode flooding could be lessened with low-humidity gas feed.

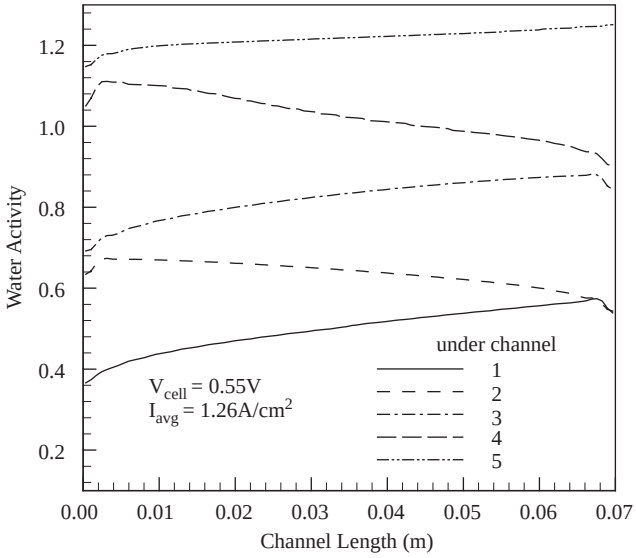

Fig. 14. Water activity profiles in the cathode catalyst layer under five gas channels at a cell voltage of 0.55 V in case 3.

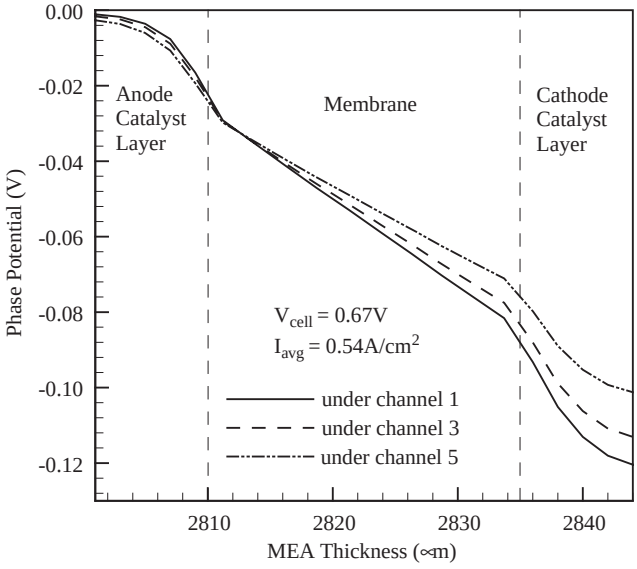

Fig. 15. Phase potential distributions across MEA under the middle of three gas channels in case 3.

Under low-humidity operation, the distribution of the current density increases with the increase of water concentration at a high cell voltage such as 0.67 V. Decreasing the cell voltage to 0.55 V with the 26 percent relative humidity in both anode and cathode inlets, the current density initially increases, but it starts to decrease after the fourth gas channel, dominated by oxygen consumption. Numerical results also reveal that the ohmic losses of proton transport in anode and cathode catalyst layers are comparable to that in the membrane in both fully and low-humidified inlet conditions and, thus the catalyst layers cannot be neglected in PEFC modeling.

This massively parallel computational method enables the exploration of a large parameter space for sensitivity analysis and design optimization of industrial-scale PEFC. Several such applications were given in Wang et al. (2002, 2003). [1]

Notation

a	water activity
c	molar concentration, mol/m^3
D	mass diffusivity, m^2/s
EW	equivalent weight of dry membrane, kg/mol
F	Faraday constant, 96 487, C/mol
j	transfer current density, A/m^3
K	permeability, m^2
M_w	molecular weight, kg/mol
n	number of electrons in electrochemical reaction
n_d	electro-osmotic drag coefficient
p	pressure, Pa
R	universal gas constant, 8.314 J/(mol K)
s	stoichiometry coefficient in electrochemical reaction
S	source term in transport equation
T	temperature, K
u	fluid velocity and superficial velocity in porous medium, m/s
U_{oc}	open-circuit potential, V

Greek letters

α	transfer coefficient
ε	porosity
η	overpotential, V
κ	ionic conductivity, S/m
λ	water content in membrane
μ	viscosity, kg/(m s)
ρ	density, kg/m^3
Φ	phase potential, V

Superscripts

eff	effective value in a porous medium
m	membrane
ref	reference value
sat	saturation value

Subscripts

a	anode
c	cathode
e	electrolyte
i	species index
m	mixture or membrane
oc	open circuit
w	water

[1] In a paper that appeared after submission of this paper, Lee et al. (2003) have also reported a computational study of water management in PEFC using STAR-CD code, however, without a detailed MEA model.

Acknowledgements

Funding for this work from DOE ultra-clean fuel program under cooperative agreement no. DE-FC26-01NT41098 is acknowledged. NSF support for a Linux PC cluster at ECEC dedicated to fuel cell and battery simulation is also acknowledged.

References

Berger, C., 1968. Handbook of Fuel Cell Technology. Prentice-Hall, Englewood Cliffs, NJ.

Bernardi, D.M., Verbrugge, M.W., 1991. Mathematical model of a gas diffusion electrode bonded to a polymer electrolyte. A.I.Ch.E. Journal 37 (8), 1151.

Bernardi, D.M., Verbrugge, M.W., 1992. A Mathematical model of the solid-polymer-electrolyte fuel cell. Journal of Electrochemical Society 139 (9), 2477.

Dutta, S., Shimpalee, S., Van Zee, J.W., 2000. Three-dimensional numerical simulation of straight channel PEM fuel cells. Journal of Applied Electrochemistry 30, 135.

Dutta, S., Shimpalee, S., Van Zee, J.W., 2001. Numerical prediction of mass-exchange between cathode and anode channels in a PEM fuel cell. International Journal of Heat and Mass Transfer 44, 2029.

Fuller, T.F., Newman, J., 1993. Water and thermal management in solid-polymer-electrolyte fuel cells. Journal of Electrochemical Society 140 (5), 1218.

Gottesfeld, S., Zawodzinski, T.A., 1997. Polymer electrolyte fuel cells, In: Alkire, R., Gerischer, H., Kolb, D., Tobias, C. (Eds.), Advances in Electrochemical Science and Engineering, Vol. 5. Wiley VCH, Weinheim, Germany, pp. 195.

Gurau, V., Liu, H., Kakac, S., 1998. Two-dimensional model for proton exchange membrane fuel cells. A.I.Ch.E. Journal 44 (11), 2410.

Lee, W.K., Shimpalee, S., Van Zee, J.W., 2003. Verifying predictions of water and current distributions in a serpentine flow field polymer electrolyte membrane fuel cell. Journal of Electrochemical Society 150 (3), A341.

Motupally, S., Becker, A.J., Weidner, J.W., 2000. Diffusion of water in nafion 115 membranes. Journal of Electrochemical Society 147 (9), 3171.

Nguyen, T.V., White, R.E., 1993. A water and heat management model for proton-exchange-membrane fuel cells. Journal of Electrochemical Society 140 (8), 2178.

Springer, T.E., Zawodzinski, T.A., Gottesfeld, S., 1991. Polymer electrolyte fuel cell model. Journal of Electrochemical Society 138 (8), 2334.

CD-Aapco Group, 2001. Star-CD Version 3.15 methodology.

Toyota Motor Corp., 2002. Private communication.

Um, S., Wang, C.Y., 2000. Three dimensional analysis of transport and reaction in proton exchange membrane fuel cells. In: Proceedings of the ASME Heat Transfer Division, Orlando, FL, Vol. 1. pp. 19–25.

Um, S., Wang, C.Y., Chen, K.S., 2000. Computational fluid dynamics modeling of proton exchange membrane fuel cells. Journal of Electrochemical Society 147 (12), 4485.

Wang, C.Y., 2003. Two-phase flow and transport in PEM fuel cells. In: Vielstich, W., Gasteiger, H., Lamm, A. (Eds.), Handbook of Fuel Cells. Wiley, New York (Chapter 32).

Wang, C.Y., Um, S., Meng, H., Pasaogullari, U., Wang, Y., 2002. Computational fuel cell dynamics (CFCD) models. In: Proceedings of 2002 Fuel Cell Seminar, Palm Springs, CA.

Wang, C.Y., Wang, G.Q., Wang, Y., Meng, H., 2003. Micro- and meso-scale phenomena in polymer electrolyte fuel cells. Presented at 2003 International Conference on Computational Nanoscience, San Francisco, CA.

Wang, Z.H., Wang, C.Y., Chen, K.S., 2001. Two-phase flow and transport in the air cathode of proton exchange membrane fuel cells. Journal of Power Sources 94 (1), 40–50.

Yi, J.S., Nguyen, T.V., 1998. A along-the-channel model for proton exchange membrane fuel cells. Journal of Electrochemical Society 145 (4), 1149.

Zhou, T., Liu, H., 2001. A general three-dimensional model for proton exchange membrane fuel cells. International Journal of Transport Phenomena 3, 177.